

Resolution of Complex Tissue Microarchitecture using the Diffusion Orientation Transform (DOT)*

Evren Özarslan^{a†}, Timothy M. Shepherd^b, Baba C. Vemuri^a,
Stephen J. Blackband^{b,c}, Thomas H. Mareci^d

^a *Department of Computer and Information Science and Engineering,
University of Florida, Gainesville, FL 32611, USA*

^b *Department of Neuroscience, University of Florida, Gainesville, FL 32610, USA.*

^c *National High Magnetic Field Laboratory, Tallahassee, FL 32310, USA.*

^d *Department of Biochemistry and Molecular Biology,
University of Florida, Gainesville, FL 32610, USA.*

*E. Özarslan, T. M. Shepherd, B. C. Vemuri, S. J. Blackband, T. H. Mareci, *Resolution of Complex Tissue Microarchitecture using the Diffusion Orientation Transform (DOT)*, University of Florida, Gainesville, FL, Technical Report TR05-004, July 2005.

†Corresponding author. E-mail: evren@cise.ufl.edu

Abstract

This article describes an accurate and fast method for fiber orientation mapping using multidirectional diffusion-weighted magnetic resonance (MR) data. This novel approach utilizes the Fourier transform relationship between the water displacement probabilities and diffusion-attenuated MR signal expressed in spherical coordinates. The radial part of the Fourier integral is evaluated analytically under the assumption that MR signal attenuates exponentially. The values of the resulting functions are evaluated at a fixed distance away from the origin. The spherical harmonic transform of these functions yields the Laplace series coefficients of the probabilities on a sphere of fixed radius. Alternatively, probability values can be computed nonparametrically using Legendre polynomials. Orientation maps calculated from excised rat nervous tissue data demonstrate this technique's ability to accurately resolve crossing fibers in anatomical regions such as the optic chiasm. This proposed methodology has a trivial extension to multiexponential diffusion-weighted signal decay. The developed methods will improve the reliability of tractography schemes and may make it possible to correctly identify the neural connections between functionally connected regions of the nervous system.

Keywords: MRI, tensor, anisotropy, HARDI, Fourier, spherical harmonics

1 Introduction

The diffusional attenuation of MR signal in pulsed field gradient experiments (Stejskal and Tanner, 1965) has been exploited to characterize diffusional anisotropy in fibrous tissues like muscle (e.g. Cleveland et al., 1976) and white-matter in animal (e.g. Moseley et al., 1990) and human (e.g. Chenevert et al., 1990) nervous tissue. When the narrow pulse condition is met, i.e. the duration of the applied diffusion sensitizing gradients (δ) is much smaller than the time between the two pulses (Δ), the fundamental relationship between the MR signal attenuation $E(\mathbf{q})$ and average displacement probabilities $P(\mathbf{R})$ is given by a Fourier integral (Callaghan, 1991):

$$P(\mathbf{R}) = \int E(\mathbf{q}) \exp(-2\pi i \mathbf{q} \cdot \mathbf{R}) d\mathbf{q}, \quad (1)$$

where \mathbf{R} is the displacement vector and \mathbf{q} is the reciprocal space vector defined by $\mathbf{q} = \gamma\delta\mathbf{G}/2\pi$, where γ is the gyromagnetic ratio and \mathbf{G} is the gradient vector.

Diffusional anisotropy is well-reflected in the water displacement probabilities and it is expected that in fibrous tissues, the orientations specified by large displacement probabilities will coincide with the fiber orientations. One could in principle estimate these displacement probability functions by using Eq. 1 and the fast Fourier transform (FFT), however this would require data points all across the space spanned by the diffusion gradients (or \mathbf{q} vectors). This q -space approach would require very high gradient strengths and long acquisition times that are difficult to achieve in clinical settings (Basser, 2002). Although attempts have been made to acquire such datasets *in vivo* (Wedeen et al., 2000), the results typically suffer from undersampled q -space and sacrificed spatial resolution.

More than a decade ago, Basser et al. (1994a,b) introduced an imaging method called diffusion tensor imaging (DTI) that replaced the apparent diffusion coefficients that had been calculated in diffusion-weighted imaging studies with a symmetric, positive-definite, second-order tensor. This model required only 7 diffusion-weighted images with clinically feasible diffusion gradient strengths. This approach enabled simple estimation of diffusional anisotropy, and predicted a fiber orientation specified by the principal eigenvector of the diffusion tensor. Despite its modest requirements, the results achieved using DTI have been very successful in regions of the brain and spinal cord with substantial white-matter coherence and have enabled the mapping of some anatomical connections in the central nervous system (e.g. Conturo et al., 1999; Mori et al., 1999; Basser et al., 2000).

DTI assumes a displacement probability characterized by an oriented Gaussian probability distribution function (PDF) whose covariance matrix is proportional to the diffusion tensor. Such a PDF has only one orientational mode and as such, can not resolve more than one fiber orientation inside a voxel. This shortcoming of DTI has prompted interest in the development of more sophisticated models. Tuch et al. (1999) introduced a high angular resolution diffusion

imaging (HARDI) method that suggested the apparent diffusion coefficients could be evaluated along many orientations independently without fitting a “global” function to the data, i.e. using the Stejskal-Tanner expression (Stejskal, 1965)

$$S(\mathbf{u}) = S_0 e^{-bD(\mathbf{u})} , \quad (2)$$

where \mathbf{u} is a unit vector specifying the direction of the diffusion sensitizing gradient, $S(\mathbf{u})$ is the signal value on a sphere in q -space whose radius is related to the diffusion weighting factor b (where $b = 4\pi q^2 t$ and $t = \Delta - \delta/3$ is the effective diffusion time), and S_0 is the signal value at $b = 0$. The result is an angular distribution of apparent diffusivities, $D(\mathbf{u})$ herein referred to as the diffusivity profile. It has been shown that the diffusivity profile has a complicated structure in voxels with orientational heterogeneity (von dem Hagen and Henkelman, 2002; Tuch et al., 2002). Several studies proposed to represent the diffusivity profile using a spherical harmonic expansion (Frank, 2002; Alexander et al., 2002). A schematic description of this approach is given below:

$$D(\mathbf{u}) \begin{array}{c} \xleftarrow{\text{LS}} \\ \xrightarrow{\text{SHT}} \end{array} a_{lm} , \quad (3)$$

where SHT and LS stand for spherical harmonic transform and Laplace series respectively.

However, one major difficulty with employing HARDI in studies involving orientation mapping has been that the peaks of the diffusivity profile do not necessarily yield the orientations of the distinct fiber populations (Figure 1). Özarslan and Mareci (2003) have shown that the (SHT) approach could be seen as a generalization of DTI since the coefficients of the Laplace series (obtained from the SHT of the diffusivity profile) are related to the components of higher-order Cartesian tensors. Later, Özarslan et al. (2004a,b) proposed to use the higher-order Cartesian tensors to generate signal values (assuming exponential attenuation) on the three-dimensional q -space, and evaluated an FFT to approximate the displacement probabilities. Jansons and Alexander (2003) proposed a method to calculate a displacement probability map from HARDI datasets by enforcing the unusual condition that the probabilities are nonzero only on a spherical shell. Although the results are encouraging, both of these schemes are computationally expensive.

Another generalization of DTI that employs higher-order Cartesian tensors was proposed by Liu et al. (2003). This approach necessitates sampling of q -space in several spherical shells, undesirably increasing the required number of acquisitions. Also, it is difficult to reliably extract the phase of the MR signal required by this scheme. Tuch et al. (2003) proposed a method in which the radial integral of the displacement PDF is approximated by the spherical Radon transform. However, the end result is the radial projection of the three-dimensional displacement PDF via a line integral and not the real probabilities as would be obtained through the radial integral with measure $r^2 dr$. More importantly, this scheme provides only an approximation

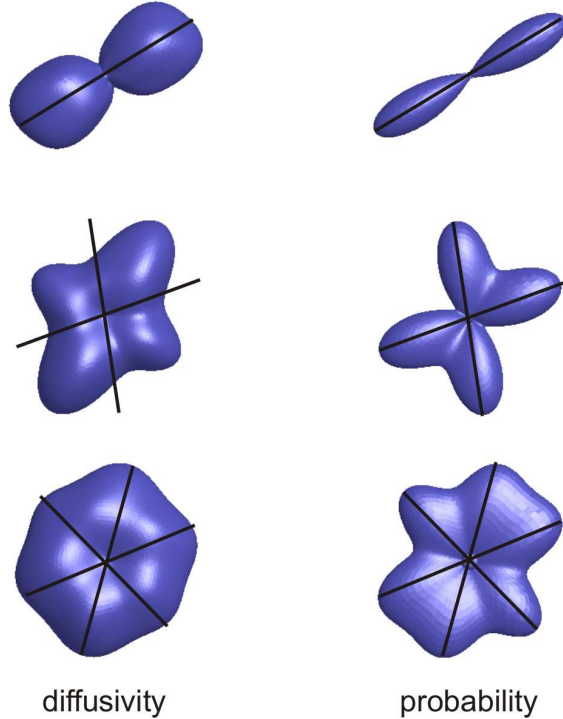


Figure 1: Apparent diffusivity (left column) and displacement probability (right column) profiles calculated from simulations of 1, 2 and 3 fiber systems (top to bottom). Black lines depict the exact orientations of the simulated fibers specified by the azimuthal angles $\phi_1 = 30^\circ$, $\phi_2 = \{20^\circ, 100^\circ\}$ and $\phi_3 = \{20^\circ, 55^\circ, 100^\circ\}$ for the 1, 2 and 3 fiber systems respectively. Polar angles for all fibers were taken to be 90° so that all fibers lie on the image plane. The peaks of the diffusivity profile do not necessarily yield the orientations of the distinct fiber populations. This can sometimes lead to erroneous fiber structure interpretation from HARDI data.

to the true radial integral because the result is a convolution of the probability values with a 0-th order Bessel function (Tuch, 2004) that gives rise to an undesirable “contamination” of the probability along one direction with probabilities from other directions. Finally, there have been several studies that have modeled diffusion using multicompartmental models. These studies assume distinct fiber populations with no exchange. Moreover, the number of such compartments has to be pre-specified (Inglis et al., 2001; Parker and Alexander, 2003; Maier et al., 2004; Assaf et al., 2004) or the signal from each fiber population is undesirably forced to have prespecified attributes (such as anisotropy) (Tournier et al., 2004).

In this work, we introduce a new method, called the diffusion orientation transform (DOT), that describes how the diffusivity profiles can be transformed into probability profiles. Our method is based on the HARDI acquisition scheme and can be extended to more general acquisition strategies. We express Eq. 1 in spherical coordinates, then under the monoexponential attenuation assumption, evaluate the radial part of the integral analytically. The probability

values on a fixed radius can be reconstructed either directly or parametrically in terms of a Laplace series. We prove that this expansion converges to the true probability profile. Our technique can be regarded as a transformation of diffusivity to probability profiles whose peaks correspond to distinct fiber orientations (Figure 1). Our method is robust and fast. Although we present results on excised, chemically-fixed rat nervous tissue, the requirements of our method make it suitable for the clinical environment. We discuss our assumption that the MR signal decays monoexponentially and further demonstrate that a trivial extension to multiexponential attenuation results in improved reconstruction of the probabilities.

2 Theory

In this section we show that starting from the signal attenuations of a HARDI acquisition, it is possible to calculate the orientation maps without the need to fit a particular model to the data. We achieve this by two different approaches.

2.1 Parametric Reconstruction

The Fourier transform that relates the signal attenuation to the water displacement probability (Eq. 1) can be written in spherical coordinates. This is a consequence of the pointwise convergent expansion of the plane wave in spherical coordinates (Schwabl, 1989) given by

$$e^{\pm 2\pi i \mathbf{q} \cdot \mathbf{R}} = 4\pi \sum_{l=0}^{\infty} \sum_{m=-l}^l (\pm i)^l j_l(2\pi q r) Y_{lm}(\mathbf{u})^* Y_{lm}(\mathbf{r}), \quad (4)$$

where $\mathbf{q} = q\mathbf{u}$ and $\mathbf{R} = r\mathbf{r}$, with $q = |\mathbf{q}|$ and $r = |\mathbf{R}|$. Inserting this expression into Eq. 1, we get

$$P(R_0\mathbf{r}) = \sum_{l=0}^{\infty} \sum_{m=-l}^l (-i)^l Y_{lm}(\mathbf{r}) \int d\mathbf{u} Y_{lm}(\mathbf{u})^* I_l(\mathbf{u}), \quad (5)$$

where

$$I_l(\mathbf{u}) = 4\pi \int_0^{\infty} dq q^2 j_l(2\pi q R_0) \exp(-4\pi^2 q^2 t D(\mathbf{u})). \quad (6)$$

Here r was set to a particular radius R_0 and it is assumed that signal attenuates along each radial line in q -space as described by the Stejskal-Tanner relationship given in Eq. 2. Note that the function $P(R_0\mathbf{r})$ is not the isosurface of the three-dimensional displacement probability function, but it is the probability of finding the particle, initially at the origin, at the point $R_0\mathbf{r}$, i.e. we will be interested in the probability values on a sphere of radius R_0 . The integral in Eq. 6 can be evaluated and it is given by

$$I_l(\mathbf{u}) = \frac{R_0^l \Gamma(\frac{l+3}{2})}{2^{l+3} \pi^{3/2} (D(\mathbf{u})t)^{(l+3)/2} \Gamma(l+3/2)} {}_1F_1\left(\frac{l+3}{2}; l+\frac{3}{2}; -\frac{R_0^2}{4D(\mathbf{u})t}\right), \quad (7)$$

Table 1: $A_l(\mathbf{u})$ and $B_l(\mathbf{u})$ functions up to $l = 8$. In this table, β stands for $\beta(\mathbf{u})$.

l	$A_l(\mathbf{u})$	$B_l(\mathbf{u})$
0	1	0
2	$-(1 + 6\beta^{-2})$	3
4	$1 + 20\beta^{-2} + 210\beta^{-4}$	$\frac{15}{2}(1 - 14\beta^{-2})$
6	$-(1 + 42\beta^{-2} + \frac{1575}{2}\beta^{-4} + 10395\beta^{-6})$	$\frac{105}{8}(1 - 36\beta^{-2} + 396\beta^{-4})$
8	$1 + 72\beta^{-2} + \frac{10395}{4}\beta^{-4} + 45045\beta^{-6} + 675675\beta^{-8}$	$\frac{315}{16}(1 - 66\beta^{-2} + 1716\beta^{-4} - 17160\beta^{-6})$

where ${}_1F_1$ is the confluent hypergeometric function of the first kind (see Appendix A). Using the recurrence relations of the confluent hypergeometric functions provided in Eqs. 30 iteratively, these functions can be written as the sum of two terms, one of them being proportional to ${}_1F_1\left(\frac{1}{2}; \frac{3}{2}; -\frac{R_0^2}{4D(\mathbf{u})t}\right)$ where the other term will be proportional to ${}_1F_1\left(\frac{3}{2}; \frac{5}{2}; -\frac{R_0^2}{4D(\mathbf{u})t}\right)$. Using Eqs. 31 and 32, it can be seen that these functions are proportional to the error function and Gaussian respectively.

Therefore, the resulting expression is given by

$$I_l(\mathbf{u}) = A_l(\mathbf{u}) \frac{\exp(-\beta(\mathbf{u})^2/4)}{(4\pi D(\mathbf{u})t)^{3/2}} + B_l(\mathbf{u}) \frac{\text{erf}(\beta(\mathbf{u})/2)}{4\pi R_0^3}, \quad (8)$$

where

$$\beta(\mathbf{u}) = \frac{R_0}{\sqrt{D(\mathbf{u})t}}. \quad (9)$$

$A_l(\mathbf{u})$ and $B_l(\mathbf{u})$ functions up to $l = 8$ are given in Table 1. Note that throughout the paper, only the even-order terms will be included as a consequence of the antipodal symmetry of the diffusivity profiles as well as displacement PDFs. The derivation of the particular forms for the $A_l(\mathbf{u})$ and $B_l(\mathbf{u})$ for arbitrary (even) values of l are provided in Appendix B.

In Figure 2a, we plot the I_l values as a function of R_0 calculated with double precision using Eq. 8 where $D = 1.5 \times 10^{-3} \text{mm}^2/\text{s}$ and $t = 25 \text{ms}$. Very large values taken by the higher-order terms near the origin are due to round-off errors. However, this is not a big concern because we will be mostly interested in the values of this function in the $10 - 20 \mu\text{m}$ range. Note that the contribution from higher-order terms is rapidly collapsing for R_0 values in this range. Shown in Figure 2b are the curves generated by keeping R_0 fixed at the value of $15 \mu\text{m}$ and varying the diffusion coefficients between 3×10^{-4} and $3 \times 10^{-3} \text{mm}^2/\text{s}$. This plot indicates the nontrivial manner in which an angular diffusivity profile influences the I_l and hence the probability values.

In order to estimate the probability on the surface of a sphere of radius R_0 , we go back to Eqs. 5 and 6. Since $I_l(\mathbf{u})$ is a function of orientation, we can expand it in a Laplace series, i.e.

$$I_l(\mathbf{u}) = \sum_{l'=0}^{\infty} \sum_{m'=-l'}^{l'} \alpha_{l'm'} Y_{l'm'}(\mathbf{u}), \quad (10)$$

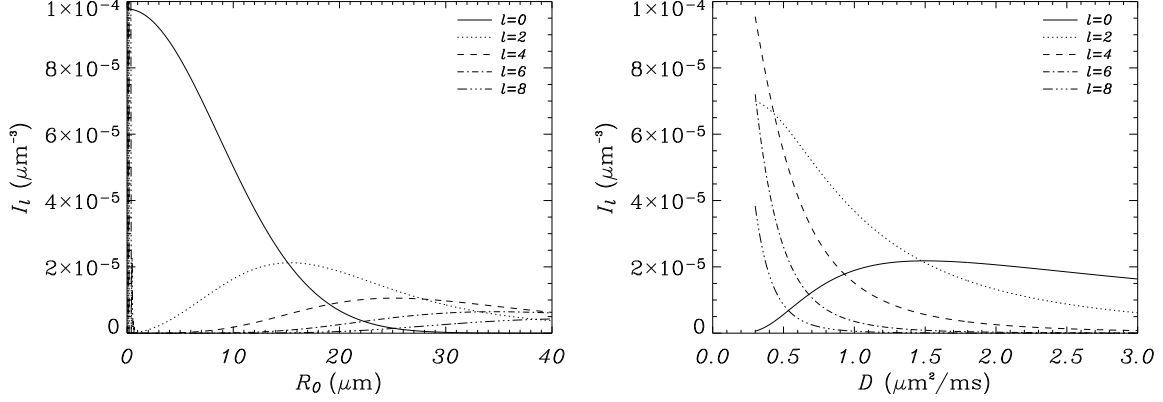


Figure 2: Dependence of the radial integral I_l on R_0 (top) and on diffusivity (bottom). The curves are drawn for l values ranging from 0 to 8.

where the coefficients $\alpha_{ll'm'}$ are given by a SHT,

$$\alpha_{ll'm'} = \int Y_{l'm'}(\mathbf{u})^* I_l(\mathbf{u}) d\mathbf{u}. \quad (11)$$

Comparing the integration over \mathbf{u} in Eq. 5 with the expression in Eq. 11, it can be seen that $P(R_0\mathbf{r})$ has the Laplace series expansion

$$P(R_0\mathbf{r}) = \sum_{l=0}^{\infty} \sum_{m=-l}^l p_{lm} Y_{lm}(\mathbf{r}) \quad (12)$$

with

$$p_{lm} = (-i)^l \alpha_{llm} = (-1)^{l/2} \alpha_{llm}, \quad (13)$$

where in the last step we have used the fact that l is even. The convergence of the resulting series in Eq. 5 to the desired probability value is proved in Appendix C. Note that the coefficients of this Laplace series for a particular value of l come from the l -th order Laplace series coefficients of $I_l(\mathbf{u})$.

2.1.1 Implementation Aspects

In summary, given the HARDI data, the estimation of the probability of finding the particle at the point $R_0\mathbf{r}$ away from the origin involves the following steps:

1. Compute the diffusivity $D(\mathbf{u})$ along each direction using Eq. 2.
2. Then compute $I_l(\mathbf{u})$ using Eq. 7 or Eq. 8 with Table 1.
3. For each l , compute α_{llm} , the l -th order spherical harmonic transform of $I_l(\mathbf{u})$.
4. Then evaluate Eq. 12.

Implementation of the items 1, 2 and 4 above are trivial. Our data acquisition scheme involves sampling the sphere on the vertices of a tessellated icosahedron. With this method 46 or 81 points are sampled on the unit hemisphere from second- or third-order tessellations respectively. Following Ritchie and Kemp (1999), we compute the spherical harmonic transform given in Eq. 11 by discretizing the integrals on the sphere with integration weights calculated from the areas of the polygons specified by the dual tessellation. We also exploit the fact that the probabilities are real. This condition ensures that the expression

$$p_{l(-m)} = (-1)^m p_{lm}^* \quad (14)$$

holds. Thus, it is unnecessary to evaluate the integrals that generate p_{lm} coefficients with negative m values. The calculation of the α_{llm} coefficients takes only 25 to 60s for the entire dataset, depending on the matrix size and number of angular samples, when using a modest Athlon XP 1800 processor (AMD, Sunnyvale, CA).

Schematic description of the method is described below. Note that this is our revision of Eq. 3 provided in the introduction.

$$D(\mathbf{u}) \xrightarrow{\text{Eq. [8]}} I_l(\mathbf{u}) \xrightarrow{\text{SHT}} \alpha_{llm} \xrightarrow{\times(-1)^{l/2}} p_{lm} \xrightarrow{\text{LS}} P(R_0\mathbf{r}) \quad (15)$$

2.2 Nonparametric Reconstruction

An alternative form to the Rayleigh expansion in Eq. 4 is given by

$$e^{\pm 2\pi i \mathbf{q} \cdot \mathbf{R}} = \sum_{l=0}^{\infty} (\pm i)^l (2l+1) j_l(2\pi q r) P_l(\mathbf{u} \cdot \mathbf{r}), \quad (16)$$

which is just a consequence of the addition theorem for spherical harmonics provided in Eq. 41. In Eq. 16, P_l is the l -th order Legendre polynomial. Employing this form of the Rayleigh expansion in our formalism does not change the radial integral and the probability values are given by

$$\begin{aligned} P(R_0\mathbf{r}) &= \frac{1}{4\pi} \sum_{l=0}^{\infty} (-i)^l (2l+1) \int d\mathbf{u} I_l(\mathbf{u}) P_l(\mathbf{u} \cdot \mathbf{r}) \\ &= \sum_{l=0}^{\infty} \int d\mathbf{u} (-1)^{l/2} \frac{2l+1}{4\pi} P_l(\mathbf{u} \cdot \mathbf{r}) I_l(\mathbf{u}), \end{aligned} \quad (17)$$

with the definition of I_l as in Eqs. 6-8.

The above expression provides an alternate estimation of the results that could be obtained from the parametric reconstruction. The schematic description of the nonparametric reconstruction is given by

$$D(\mathbf{u}) \xrightarrow{\text{Eq. 8}} I_l(\mathbf{u}) \xrightarrow{\text{Eq. 17}} P(R_0\mathbf{r}) \quad (18)$$

The above formulation can be easily expressed in matrix form. Suppose that the HARDI experiment is performed with diffusion sensitizing gradients applied along N_G directions. The direction describing the j -th gradient will be represented with the unit vector \mathbf{u}_j . Similarly, let \mathbf{r}_i denote the unit vector describing the i -th direction along which the probability will be estimated where the total number of such directions is N_R . Then Eq. 17 can be expressed simply by

$$\mathbf{Y} = \sum_{l=0}^{\infty} \mathbf{M}_l \mathbf{Z}_l, \quad (19)$$

where \mathbf{Y} is the N_R dimensional vector of probabilities. In Eq. 19 the components of the N_G dimensional vector \mathbf{Z}_l are given by

$$(\mathbf{Z}_l)_j = I_l(\mathbf{u}_j), \quad (20)$$

and the components of the $N_R \times N_G$ dimensional matrix \mathbf{M}_l are given by

$$(\mathbf{M}_l)_{ij} = \frac{w_j}{4\pi} (-1)^{l/2} (2l+1) P_l(\mathbf{u}_j \cdot \mathbf{r}_i), \quad (21)$$

where w_j are the integration weights associated with each of the gradient directions. Note that the matrices \mathbf{M}_l can be computed once for each gradient sampling scheme. Therefore, the only computational burden comes from the pixel-by-pixel estimation of $I_l(\mathbf{u}_j)$ (which is a straightforward operation) and the matrix multiplication in Eq. 19.

2.3 Parametric vs. Nonparametric Reconstruction

We have provided two methods for the reconstruction of probability profiles. The parametric reconstruction enables one to express the probabilities in terms of a Laplace series, whereas the nonparametric reconstruction provided the probability values directly. It is simpler to implement the latter scheme as no SHT transform is necessary. However, when the Laplace series is terminated at $l = l_{\max}$, the parametric reconstruction expresses the probability values in terms of $(l_{\max}+1)(l_{\max}+2)/2$ numbers, which are typically much smaller than the number of directions along which the probabilities are estimated (N_R) when one visualizes the probability surfaces. This enables more feasible storage of the probability profiles in computer memory.

Using either one of the schemes, once the probability values are evaluated along many points, the following parametrized surface can be visualized (see Fig. 1):

$$\mathbf{X}(\theta, \phi) = P(R_0 \mathbf{r}) \mathbf{r} = P(\theta, \phi) \begin{pmatrix} \sin \theta \cos \phi \\ \sin \theta \sin \phi \\ \cos \theta \end{pmatrix}, \quad (22)$$

where θ is the polar and ϕ is the azimuthal angle associated with the unit vector \mathbf{r} .

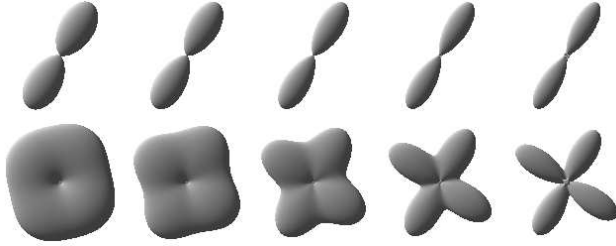


Figure 3: Probability maps estimated on a sphere of radius 8 to $16\mu m$ in equal steps of $2\mu m$ (from left to right.) Top row shows these surfaces when there is only one orientation, where the bottom row shows them from a voxel with two distinct orientations. As the radius of the sphere on which the probability values are estimated is increased, the two fiber orientations are better resolved.

3 Simulations

We have applied the scheme described above to the simulations of single fiber and crossing fiber systems. The simulations employed the exact form of the MR signal attenuation from particles diffusing inside cylindrical boundaries (Söderman and Jönsson, 1995) with parameters provided in Özarslan et al. (2005). As already shown in Figure 1, we have computed the probability profiles from fiber configurations whose fiber orientations are specified by the azimuthal angles $\phi_1 = 30^\circ$, $\phi_2 = \{20^\circ, 100^\circ\}$ and $\phi_3 = \{20^\circ, 55^\circ, 100^\circ\}$ for the 1, 2 and 3 fiber systems respectively. Polar angles for all fibers were taken to be 90° so that a view from the $+z$ -axis will clearly depict the individual fiber orientations. Computations with other polar angles yielded similar quality results. In all computations, the Laplace series were terminated after $l = 8$.

Figure 3 shows the effect of varying R_0 on the constructed probability surfaces. Increasing R_0 gives rise to the sharpening of the displacement PDFs. This could be predicted from Fig. 2a that indicates that for small R_0 the largest contribution comes from I_0 , which upon the spherical harmonic transform forms the isotropic part of the constructed probabilities. When R_0 is greater than the radius of the cylinder confining the water molecules and the characteristic length $\sqrt{6Dt}$ associated with the diffusion process (which is $15\mu m$ for the system in Figure 2a), the distribution of probability on the surface becomes sharper and individual fiber populations are better resolved.

We also computed the probability surfaces for a simulated image of fiber crossings shown in Figure 4. The surfaces are consistent with the underlying known fibrous structure. The circular and linear fiber bundles were chosen so that a distribution of crossing angles is achieved across the region with orientational heterogeneity. We notice that distinct fiber orientations are better resolved when the different fiber bundles make larger angles with each other. Fig. 4b shows the probability profiles when there is no noise added to the signal values. Similar to Jansons

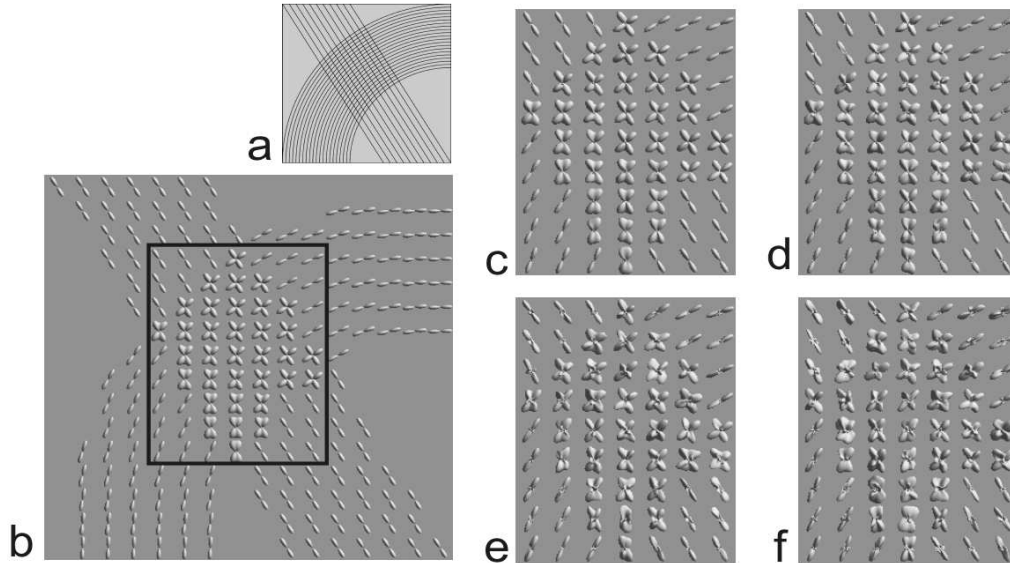


Figure 4: (a) Simulated system of two crossing fiber bundles. (b) Probability surfaces computed using the expansion of the probability on the surface of a sphere. (c-f) Surfaces in the framed area of panel b recomputed under increasing levels of noise added to the signal values. These panels represent images with signal-to-noise ratios (SNRs) between 50:1 and 12.5:1 in the non-diffusion-weighted image.

and Alexander (2003), we have added Gaussian noise of increasing standard deviation to the real and complex parts of the signal. When the signal intensity in the image with no diffusion weighting is taken to be centered around 1, and Gaussian noise of standard deviations 0.02 through 0.08 is added (in equal steps), the probability profiles shown in Fig. 4c-f are obtained. These panels represent images with signal-to-noise ratios (SNRs) between 50:1 and 12.5:1 in the non-diffusion-weighted (S_0) image. Note that in our standard HARDI protocol, we obtain SNR values in excess of 30 in diffusion-weighted scans and about 100 in non-diffusion-weighted images. Therefore, in real experiments, one can expect to achieve results that will be of similar or better quality with the image presented in Fig. 4c.

To provide a more quantitative assessment of the DOT method and its sensitivity to increasing noise levels, we took the HARDI simulations of 1, 2 and 3 fiber profiles presented in Figure 1 and numerically computed the fiber orientations by finding the maxima of the probability profiles (see Table 2). In this table, ψ denotes the angle between the computed and the true fiber orientations in degrees whereas σ is the noise level. Note that when no noise was introduced ($\sigma = 0$), there was a small deviation of the computed fiber direction from the true fiber orientation because of the finite sampling of the hemisphere (at 81 gradient orientations), the termination of the LS at order 8 and the precision of the numerical procedure used to compute the maxima of the probability profiles. The simulations of the signal profiles with noise were

Table 2: The angle between the computed and true fiber orientations (deviation angles) in degrees. Second column presents the deviation angle of each fiber when the DOT of noiseless signal profile is taken. Columns 3-6 show the mean and standard deviation values for the deviation angle when Gaussian noise of standard deviation 0.02 to 0.08 (from left to right) was added to the signal profiles. The computations for the DOT of noisy signals were repeated 100 times.

	$\psi(\sigma = 0)$	$\psi(\sigma = 0.02)$	$\psi(\sigma = 0.04)$	$\psi(\sigma = 0.06)$	$\psi(\sigma = 0.08)$
1 fiber	{0.364}	0.77 ± 0.42	1.44 ± 0.79	2.20 ± 1.09	3.08 ± 1.66
2 fibers	{1.43, 0.80}	2.33 ± 1.10	3.66 ± 2.01	6.00 ± 5.57	8.07 ± 7.92
3 fibers	{2.87, 0.60, 4.57}	5.81 ± 5.84	11.5 ± 10.1	14.7 ± 10.3	17.6 ± 11.9

repeated 100 times for each noise level to provide a distribution of deviation angles. We report the mean and standard deviations of these distributions in columns 3-6 of Table 2. As expected, the ψ values increase with increasing noise and it is more challenging to accurately resolve the distinct fiber orientations when there are more fiber orientations.

4 Imaging Parameters

To test the performance of the DOT, we calculated the orientation probabilities on HARDI data from three anatomical regions of excised, perfusion-fixed rat nervous tissue (optic chiasm, brain and spinal cord). These experiments were performed with the approval of the University of Florida Institutional Animal Care and Use Committee. The images were acquired at $17.6T$ (brain) or $14.1T$ (spinal cord and optic chiasm) using Bruker Avance imaging systems. A diffusion-weighted spin echo pulse sequence was used. Diffusion-weighted images were acquired along 81 (brain) or 46 (spinal cord and optic chiasm) directions with a b -value of $1500s/mm^2$ (brain and spinal cord) or $1250s/mm^2$ (optic chiasm) along with a single image acquired at $b \approx 0s/mm^2$. Echo times were 23, 28, $25ms$; repetition times were 0.5, 2, $1.17s$; Δ values were 12.4, 17.8, $17.5ms$; δ values were 1.2, 2.2, $1.5ms$; bandwidth was set to 35, 32, $39kHz$; signal averages were 10, 6, 7; matrix sizes were $128 \times 128 \times 5$, $100 \times 100 \times 60$, $72 \times 72 \times 40$ and resolutions were $33.6 \times 33.6 \times 200\mu m^3$, $150 \times 150 \times 300\mu m^3$, $60 \times 60 \times 300\mu m^3$ for optic chiasm, brain and spinal cord data respectively. The optic chiasm images were signal averaged to $67.2 \times 67.2 \times 200\mu m^3$ resolution prior to probability calculations. In Figure 5 we show a particular axial slice from a HARDI dataset collected from excised rat spinal cord.

5 Scalar Indices

Many clinical studies employ scalar rotationally invariant measures derived from diffusion MRI data to quantify the changes occurring with development and pathologies. Recently, Özarlan

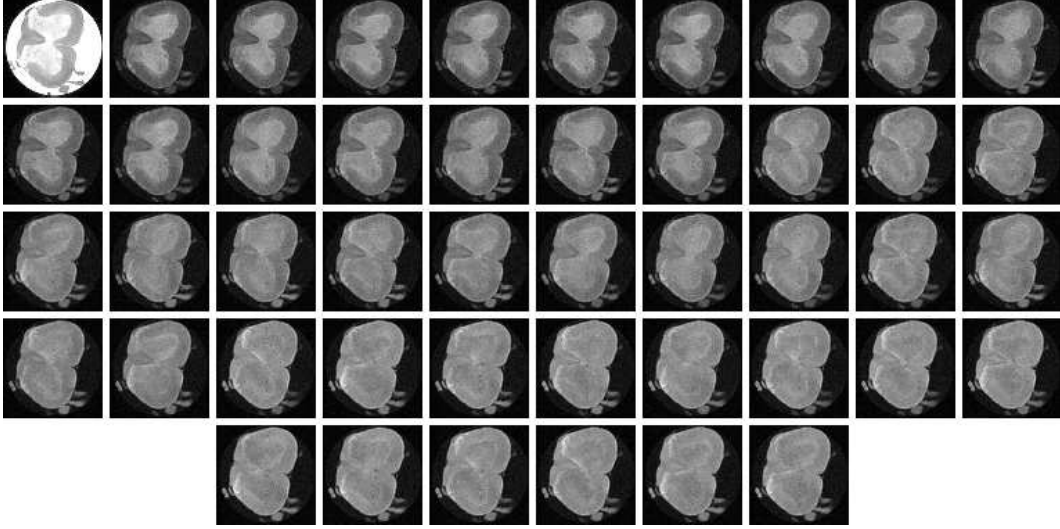


Figure 5: Representative HARDI data set from an excised, perfusion-fixed rat spinal cord. At the upper left corner is the image with no diffusion weighting followed by 45 diffusion-weighted images.

et al. (2005) demonstrated that generalized models more accurately quantify anisotropy measures compared to DTI. In this section, we discuss the estimation of the generalized scalar indices from the probability values evaluated using DOT, and demonstrate the images constructed by computing these measures on a pixel-by-pixel basis. For completeness, formulation of anisotropy in terms of both variance and entropy are provided.

5.1 Anisotropy from Variance

In Özarslan et al. (2005) generalized anisotropy indices based on the variance of the values of an arbitrary integrable positive-definite function defined on the unit sphere were presented. When applied to functions represented in terms of spherical harmonics, like the parametrically reconstructed $P(R_0\mathbf{r})$ in this work, the variance takes a particularly simple form given by

$$V = \frac{1}{9p_{00}^2} \sum_{l=2}^{\infty} \sum_{m=-l}^l |p_{lm}|^2. \quad (23)$$

Then, using the scaling relationship provided in Özarslan et al. (2005), it is possible to map the values of the variance to the interval $[0, 1)$ where the resulting index is called generalized anisotropy (GA).

5.2 Anisotropy from Entropy

The function defined on the sphere can be taken as a PDF simply by normalizing the integral of the probability profile over the sphere via a multiplication of the p_{lm} coefficients by $1/\sqrt{4\pi}p_{00}$.

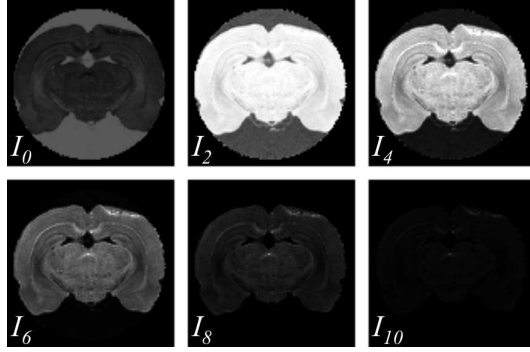


Figure 6: $I_l(\mathbf{u})$ images up to $l = 10$ from coronal sections of rat brain when \mathbf{u} is chosen to point through the image plane.

Then, it is meaningful to define the entropy associated with this distribution. By using the expression in Özarslan et al. (2005) for the entropy of a general function on the unit sphere, it is possible to show that the entropy in our case is given by¹

$$\begin{aligned}
 \sigma &= \ln(4\pi \langle P(R_0\mathbf{r}) \rangle) - \frac{1}{4\pi \langle P(R_0\mathbf{r}) \rangle} \int d\mathbf{u} P(R_0\mathbf{r}) \ln P(R_0\mathbf{r}) \\
 &= \ln(\sqrt{4\pi} p_{00}) - \frac{1}{\sqrt{4\pi} p_{00}} \sum_{l=0}^{\infty} \sum_{m=-l}^l p_{lm}^* \lambda_{lm}, \tag{24}
 \end{aligned}$$

where λ_{lm} are given by the SHT of $\ln P(R_0\mathbf{r})$. Similar to the transformation of variance values into the GA index, the entropy values can be transformed into an anisotropy index that was called scaled entropy (SE) (Özarslan et al., 2005).

6 Results

The probability maps were calculated by following the procedure described in the theory section. Terms up to $l = 8$ were included in all calculations. Representative images of the $I_l(\mathbf{u})$ values, when \mathbf{u} is chosen to point through the image plane, are presented in Figure 6. Note that the intensity values in the $I_{10}(\mathbf{u})$ image are very small. The p_{lm} coefficients that generate the probability surfaces are shown in Fig. 7 for the same slice. It was not necessary to show the coefficients with negative m values because of Eq. 14. Note that this relationship also ensures that p_{l0} are real.

The computed p_{lm} components were used in the calculation of the scalar measures described in the previous section. In Figure 8, we show the variance and GA maps computed from the optic chiasm and brain datasets. The GA index was calculated both from the p_{lm} coefficients

¹The expression for the entropy is a slightly modified version of the expression in Özarslan et al. (2005), where the 3 in the argument of the natural logarithm is replaced by 4π . The reason for this modification stems from the difference between the normalization conditions imposed on the functions $D_N(\mathbf{u})$ in Özarslan et al. (2005) and $P(R_0\mathbf{r})$ in this work.

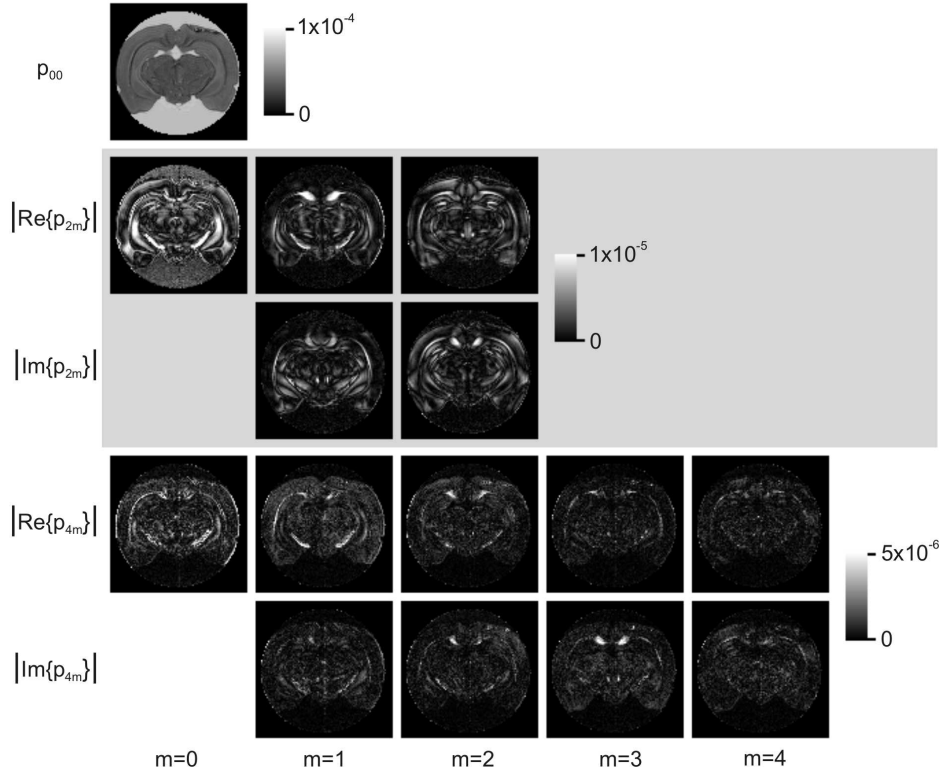


Figure 7: The LS coefficients of the probability profile up to $l = 4$ computed from the excised rat brain data set.

and a second-order tensor fit to the data. It is apparent that although the GA values are similar in the unidirectional section of the optic chiasm, in the region of decussating optic nerve fibers, GA values implied by DTI were lower than those calculated from the probability surfaces. Also included are the entropy (σ) and the SE maps calculated from both samples. It should be noted that V , GA, σ and SE values depend on the choice of R_0 .

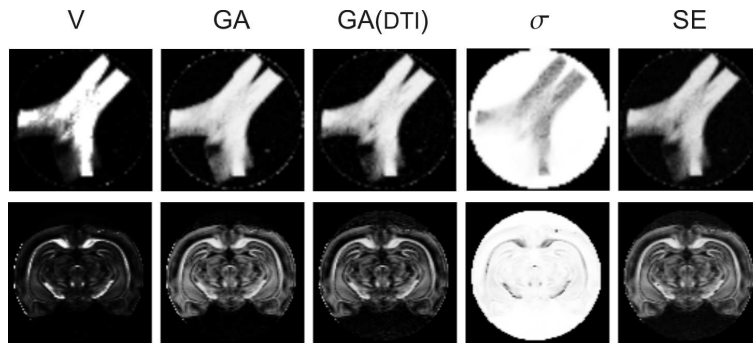


Figure 8: From left to right: Variance, GA, GA from the rank-2 tensor, entropy and SE images calculated for excised rat optic chiasm (top) and brain (bottom) samples.

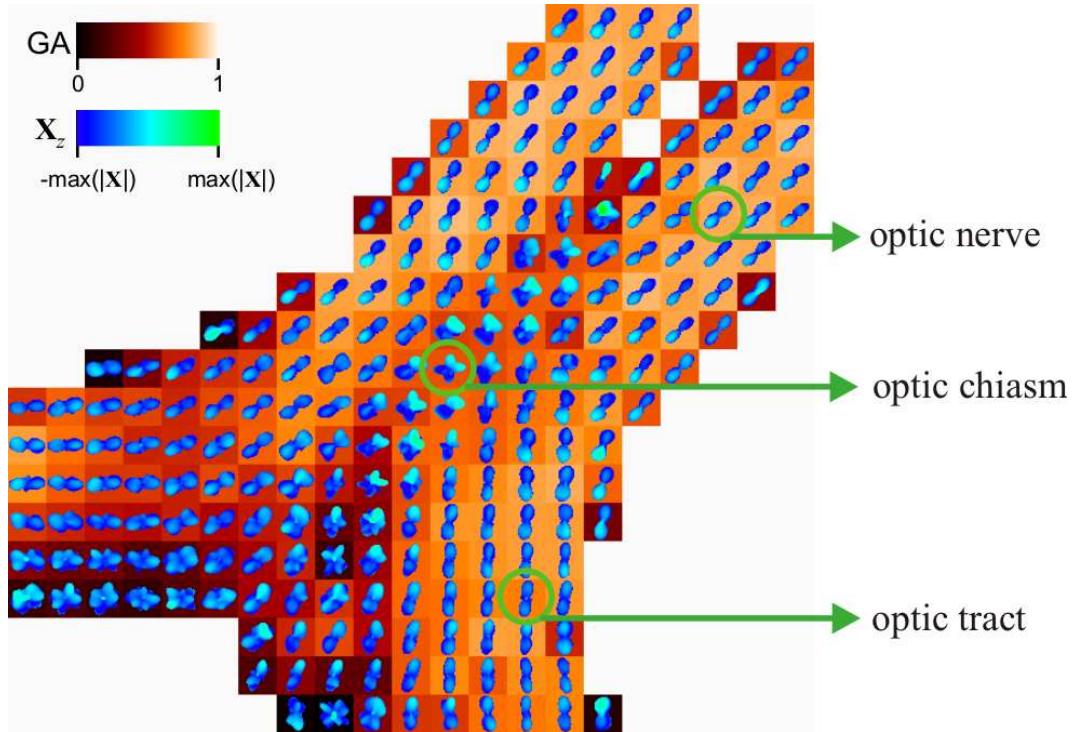


Figure 9: Probability maps calculated from a rat optic chiasm data set overlaid on an axially-oriented GA map. The decussations of myelinated axons from the two optic nerves at the center of the optic chiasm are readily apparent using the DOT method. These crossing fibers carry information from the temporal visual fields to the contralateral hemispheres. In figures 9 through 12, the orientation surfaces are color-coded such that portions of the surfaces pointing towards or away from the reader are green and blue respectively (see inset).

Visualization of the probability profiles was done by computing the probabilities along many directions and displaying the parametrized surface defined in Eq. 22. To increase the sharpness of the probability profiles, we have subtracted the minimum probability existing in the profile from all probability values. This process was followed by a normalization of the surface to fill the cube (voxel) it will be located in so that all visualized surfaces have similar sizes. As a result, the visualized surfaces emphasize the directionality, but are not intended to provide information on the true values for the probabilities.

We have overlaid these orientation surfaces on generalized anisotropy (GA) maps (Özarslan et al., 2005) computed from the displacement probabilities shown above. The coloring schemes proposed for DTI orientation visualization (Pajevic and Pierpaoli, 1999) are not readily applicable to probability surfaces. The “peakedness” on the image plane is obvious. However, one may miss the orientations through the image plane. To prevent this, we color-coded the surfaces such that as the values of the z -component of the parametrized surface vary from the maximum probability value present in the probability profile to minus this maximum probability value,

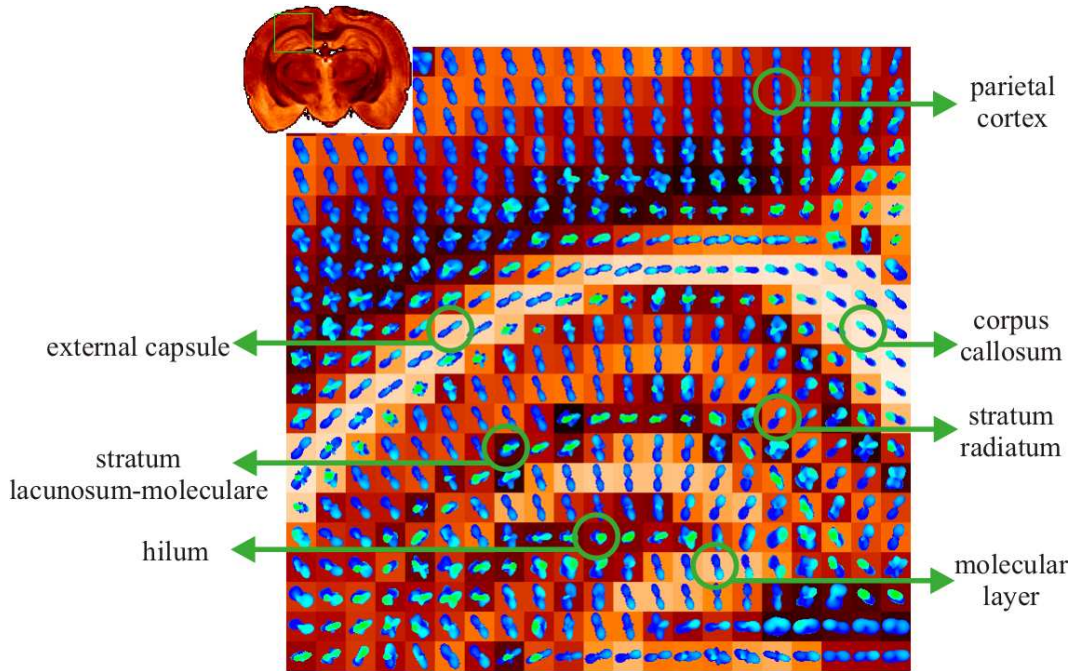


Figure 10: Probability map of a coronally-oriented GA image of the rat brain. Diffusion fiber orientations in the parietal cortex were collinear with the apical dendrites and axons of cortical pyramidal neurons found in cortical layers III-V. In the dorsal hippocampus, the molecular layer and stratum radiatum fiber orientations paralleled the apical dendrites of granule cells and pyramidal neurons respectively, whereas in the stratum lacunosum-moleculare orientations paralleled Schaffer collaterals from CA1 neurons and perforant fibers from the entorhinal cortex.

the color of the surface changes from green to blue. In all calculations R_0 was set to $16\mu m$, and the last term kept in the Laplace series was $l = 8$.

The rat optic chiasm is a distinct white matter structure with both parallel and decussating optic nerve fibers, thus providing an excellent experimental validation for our approach. Figure 9 shows the displacement probabilities computed from the optic chiasm image where every other pixel was included for the sake of clarity. This figure demonstrates the distinct fiber orientations in the central region of the optic chiasm where myelinated axons from the two optic nerves cross one another to reach their respective contralateral optic tracts.

Figure 10 shows the displacement probabilities calculated from excised coronal rat brain MRI data. At the top left is a diffusion-weighted image that shows the selected ROI. This region is expanded in the large image and depicts the orientations of the highly anisotropic and coherent fibers of the external capsule and corpus-callosum bordered inferiorly by the hippocampus and superiorly by radial cortical trajectories. Note, voxels with crossing orientations located superiorly to the external capsule represent the interdigitation of fibers entering the cortex from the external capsule and the corpus callosum into the radial orientations of the cor-

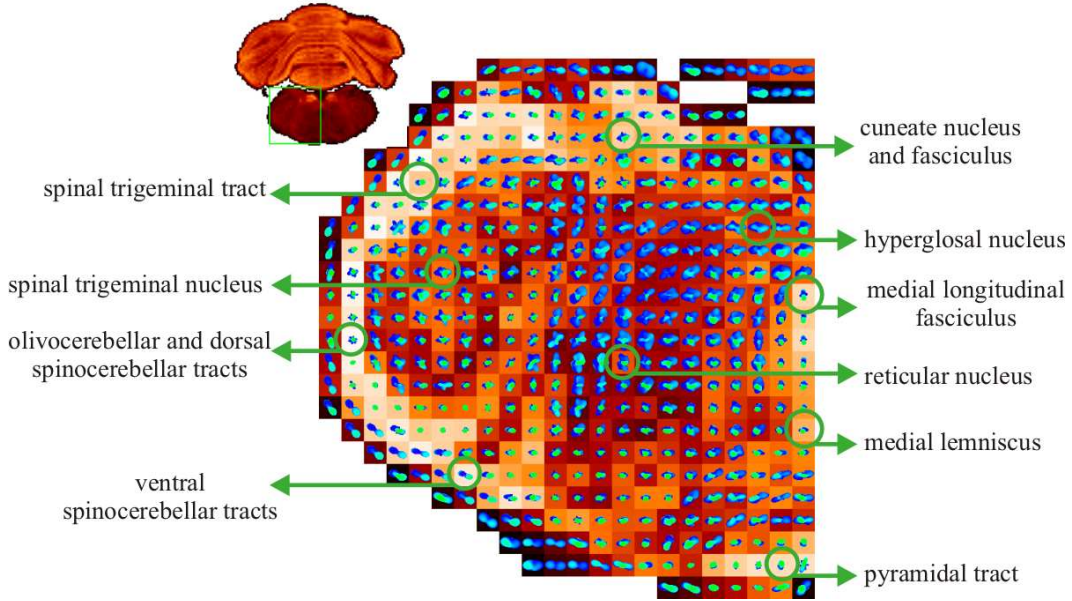


Figure 11: The Diffusion Orientation Transform (DOT) described in this paper also characterized the complex cytoarchitecture of the rat brainstem well as shown in this probability map from one side of the rat medulla.

tex. Future investigations employing this method should improve our understanding of normal and pathologically-altered neuroanatomy in regions of complex fiber architecture such as the rat brainstem (Figure 11).

Finally, we show the probability maps computed from excised spinal cord data in Figure 12. Again the ROI is specified on a diffusion-weighted image shown on the top left section. The corresponding orientation maps are depicted in the top right panel. Selected pixels of this image were enlarged on the bottom panels of the figure. To demonstrate the shapes more clearly, seven selected surfaces were rotated by -90° about the x -axis so that the up-and-down direction in the individual surfaces shown in blue correspond to in-and-out direction in red images. The magnified surfaces may represent locations where ventral root fibers from α -motor neurons cross white matter to enter the gray matter of the spinal cord.

7 Discussion

7.1 Exponential Attenuation Assumption

We have assumed so far that the signal attenuation along each radial line in q -space is characterized by an monoexponential decay. Therefore, it was possible to extract orientational information from data acquired on a single spherical shell and at the origin of the q -space. We would like to note that this is the very assumption that is intrinsic to DTI, establishing the correspondence between the diffusion tensor and the assumed Gaussian PDF whose orienta-

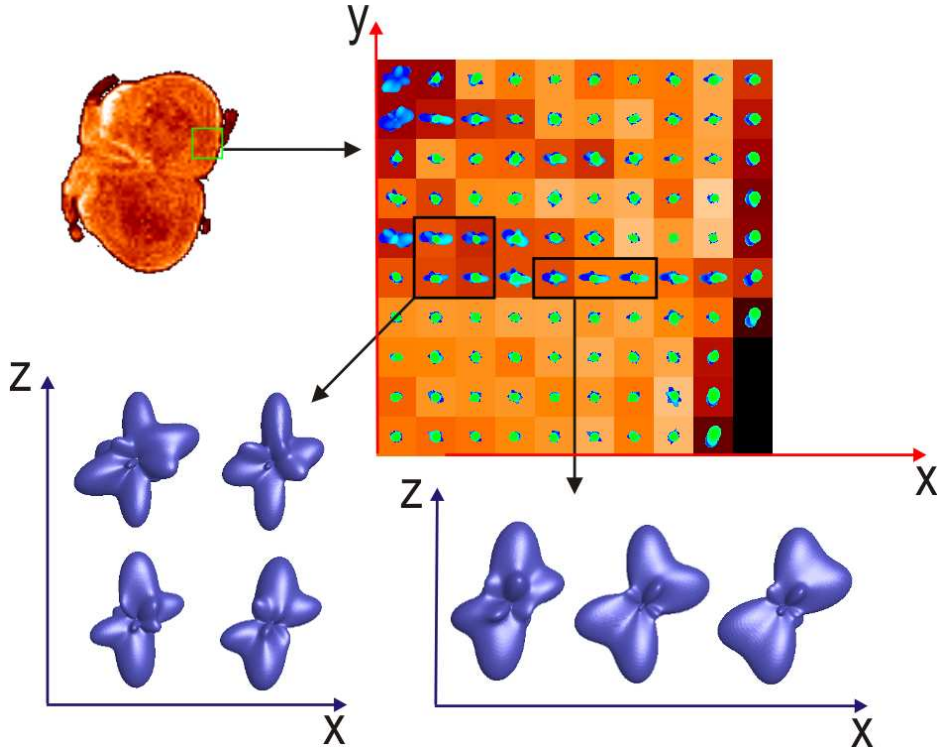


Figure 12: Probability maps calculated from a diffusion-weighted dataset acquired from an excised rat spinal cord. The surfaces in the bottom row depict the probability profiles selected from the image matrix and rotated -90° about the x -axis. These crossing fiber orientations may represent coherent ventral root spinal nerve fibers penetrating along the x -axis perpendicular to ascending and descending white matter axons in the anterior funiculus to reach the anterior horn motor neurons.

tional mode is estimated from the principal eigenvector of the diffusion tensor. The satisfactory performance of DTI in systems with single fiber orientations has prompted us to keep the monoexponentiality assumption for the radial behavior while complicating the angular structure; this results in non-Gaussian probability profiles. This assumption worked with our simulations and with real datasets.

In Figure 13, we show simulated signal values from a one fiber system with a fiber radius of $10\mu m$ when the angle between the fiber orientation and the gradient direction varies between 0° and 90° in steps of 30° . Also shown are the signal values assumed by the exponentiality assumption when the experiment is performed at $b = 1500 s/mm^2$. Note that this is a logarithmic plot, therefore the true deviations between the real and assumed signal values are much smaller than what they appear on the right side of the plot when the signal values are small. Because the q -space is the frequency space for the probabilities, from a signal processing point-of-view the exponentiality assumption can be thought of as a low-pass filtering of the true probability values. Therefore, the result is a broadened PDF. A correction scheme for this effect is described

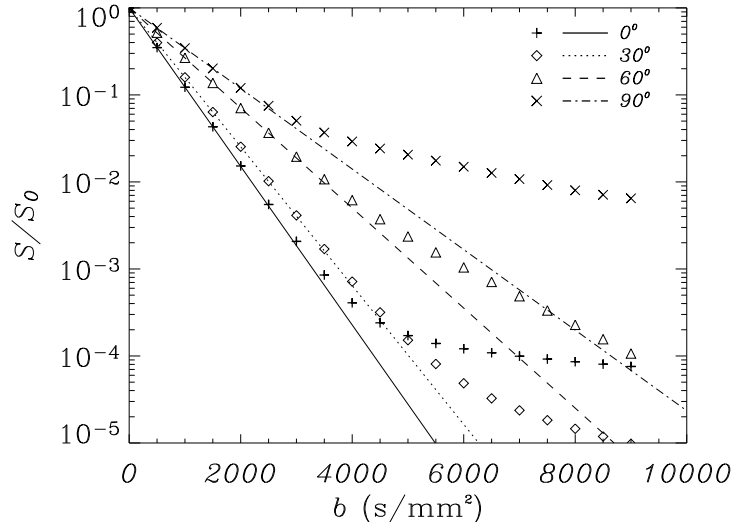


Figure 13: Logarithmic plot of the signal attenuation values as a function of the b -value. The symbols indicate the signal attenuations calculated from a simulation of a single fiber system while the lines indicate the monoexponential fits when the HARDI experiment is performed at a b -value of 1500 s/mm^2 . The curves correspond to different angles between the diffusion gradient and fiber orientations.

below.

We also have investigated the effect of b -value on the constructed probability surfaces. To this end, we simulated HARDI experiments performed at increasing b -values on 1 and 2 fiber systems. We also repeated the simulations for fibers of radii 5 and $10\ \mu\text{m}$. The selected results are provided in Figure 14. The most reassuring finding is that there has been no realizable alteration in the peaks of the distributions indicating that the calculated fiber orientations are robust to the choice of b -value. However, it is evident that the probability surfaces are sharper and multiple orientations are better resolved at higher b -values. As we have demonstrated before, a b -value of $1500\ \text{s/mm}^2$ seems sufficient to resolve the fiber crossings when the radii of the fibers are $5\ \mu\text{m}$. However, when the radii are doubled, it is advantageous to collect the data at higher b -values. It should be noted that spurious peaks start to develop at very high b -values (see the first two rows of the last column). This may be explained by the crossing of the signal decay curves in Figure 13, which suggests that at high b -values the order of signal values from different orientations may be altered.

7.2 Extension to Multiexponential Attenuation

We have thus far employed the monoexponentiality assumption of the signal attenuation. However, the same formalism provides a surprisingly simple extension to multiexponential attenua-

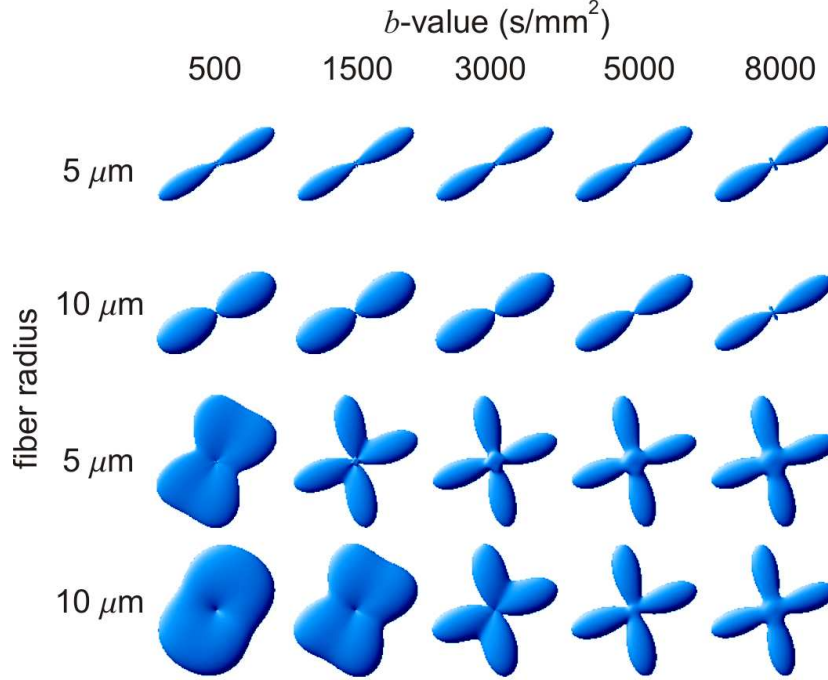


Figure 14: Simulations of 1 and 2 fiber systems as a function of b -value where the radii of the fibers were taken to be 5 and 10 μm .

tion², which has been shown in numerous articles to provide a very accurate characterization of the radial behavior (in q -space) of the MR data collected from tissue (e.g. Niendorf et al., 1996).

To derive the correct generalization, we start by replacing the Stejskal-Tanner equation (Eq. 2) with the expression:

$$\frac{S(b, \mathbf{u})}{S_0} = \sum_i^{N_E} f_i(\mathbf{u}) e^{-bD_i(\mathbf{u})}, \quad (25)$$

where N_E is the number of terms (exponentials, transients) in the series, $D_i(\mathbf{u})$ is the i -th diffusion coefficient for the gradient direction \mathbf{u} , and $f_i(\mathbf{u})$ is the “volume fraction” of the i -th exponential satisfying the relationship

$$\sum_i^{N_E} f_i(\mathbf{u}) = 1. \quad (26)$$

Carrying out the same algebra as before, Eqs. 5 and 17 hold with the definition

$$I_l(\mathbf{u}) = \sum_{i=1}^{N_E} f_i(\mathbf{u}) I_{li}(\mathbf{u}), \quad (27)$$

²We would like to stress that we utilize the multiexponential fit solely to provide an approximation and extrapolation to the signal attenuation and by no means do we intend to make inferences about the compartmentation in tissue from this fit.

where

$$I_{li}(\mathbf{u}) = 4\pi \int_0^\infty dq q^2 j_l(2\pi q R_0) \exp(-4\pi^2 q^2 t D_i(\mathbf{u})) , \quad (28)$$

which is the same expression when $D(\mathbf{u})$ in Eq. 6 is replaced by $D_i(\mathbf{u})$. Therefore, either of the forms given in Eqs. 7 or 8 can still be used to calculate $I_{li}(\mathbf{u})$ from $D_i(\mathbf{u})$.

The extension to multiexponential attenuation requires the following modifications to the implementation of the DOT:

1. Fit multiexponential function (Eq. 25) along each radial line in q -space to estimate $f_i(\mathbf{u})$ and $D_i(\mathbf{u})$.
2. For each diffusion coefficient $D_i(\mathbf{u})$ corresponding to each term in the series, calculate $I_{li}(\mathbf{u})$ from Eq. 28.
3. Calculate $I_l(\mathbf{u})$ from Eq. 27.
4. Apply either the parametric or nonparametric reconstruction as before.

Figure 15 shows the biexponential fits to the data points already presented in Figure 13. The improvement in the functional fits is evident.

We have tested the proposed extension scheme on our simulated data from 1, 2 and 3 fiber systems. The results are shown in Figure 16. It is clear that the monoexponential and multiexponential fits provide the same orientational information, yet the constructed probability

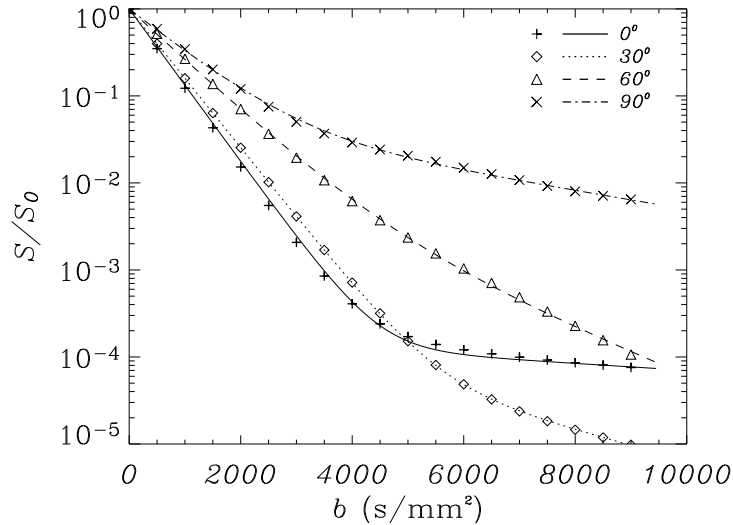


Figure 15: The symbols indicate the signal attenuations calculated for the same system as in Figure 13 whereas the lines indicate the curves obtained from a biexponential fit to these data points. The curves correspond to different angles between the diffusion gradient and fiber orientations.

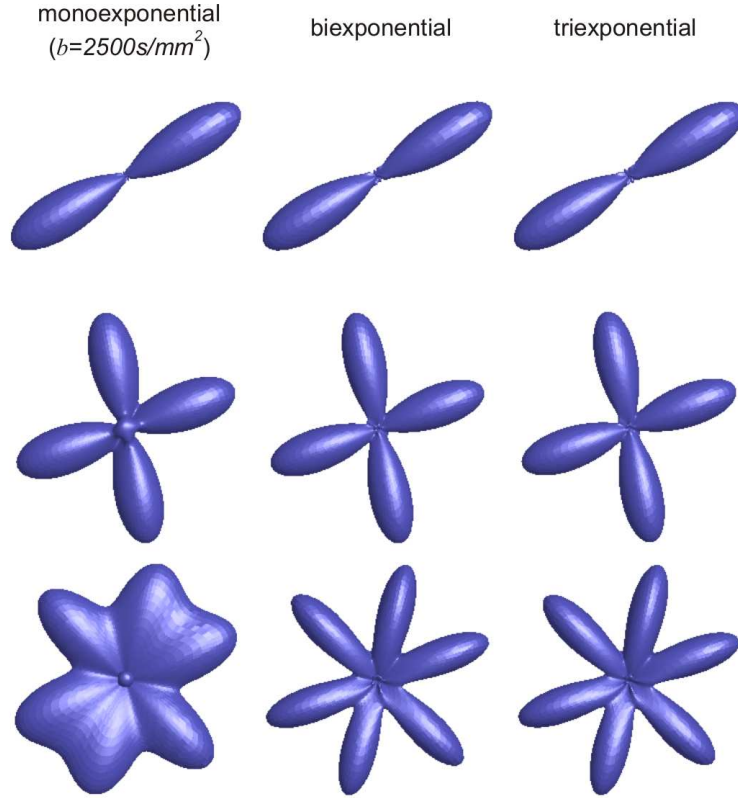


Figure 16: Simulations of 1, 2 and 3 fiber systems with mono- ($b = 2500s/mm^2$), bi- and triexponential fits (from data up to $b = 9000s/mm^2$). Similar to Figure 1, the orientations of the simulated fibers are specified by the azimuthal angles $\phi_1 = 30^\circ$, $\phi_2 = \{20^\circ, 100^\circ\}$ and $\phi_3 = \{20^\circ, 55^\circ, 100^\circ\}$ for the 1, 2 and 3 fiber systems respectively. All fibers lie on the image plane.

surfaces in the latter case resolve the distinct fiber orientations better, most notably in the 3 fiber system. However, the results indicate that transition from bi- to triexponential fits does not result in a significant improvement. This demonstrates the sufficient accuracy of the biexponential fits to the signal attenuation values.

Unfortunately, using a biexponential attenuation fit in our formalism would necessitate collecting about three times the number of data points when compared with the case in which the monoexponentiality assumption is made. This is because there are $2 * N_E$ unknowns in the fit, and if one chooses to collect data at $b = 0$, then $2 * N_E - 1$ spherical shells have to be sampled for the N_E -exponential fits.

8 Conclusion

The DOT technique provides a direct estimation of displacement probability surfaces within each voxel from multi-orientational diffusion-weighted MRI data. The method is robust and

fast. DOT can be implemented non-parametrically for direct estimation of probability values along desired directions, or by using an SHT that gives the Laplace series coefficients of the probability profile. In either case, high resolution probability surfaces can be reconstructed easily from the signal values. Further, the behavior of the MR signal intensities with increasing b -values can be characterized by mono- or multiexponential fits. Our findings indicate that multiexponential fits result in higher quality reconstructions. However, when the acquisition time or the available gradient strength is limited, the monoexponentiality assumption can be employed that results in some broadening of the PDF whose angular structure is smoother. As demonstrated in excised rat nervous tissue, the potential applications of our approach include more accurate estimates of fiber orientations that will improve the existing fiber tractography schemes and enable the reliable mapping of more neural connections between different parts of fibrous tissues.

Acknowledgments

All MRI data was obtained at the Advanced Magnetic Resonance Imaging and Spectroscopy (AMRIS) facility in the McKnight Brain Institute at the University of Florida. This research was supported by the National Institutes of Health Grants R01-NS42075, R01-NS36992 and P41-RR16105, and the National High Magnetic Field Laboratory (NHMFL), Tallahassee.

Appendix A. Confluent Hypergeometric Functions of the First Kind

The confluent hypergeometric function of the first kind (also known as Kummer's function of the first kind or Kummer's function) ${}_1F_1(a; b; x)$ is given by the series (Abramowitz and Stegun, 1977)

$${}_1F_1(a; b; x) = \sum_{k=0}^{\infty} \frac{(a)_k x^k}{(b)_k k!}, \quad (29)$$

where $(a)_k = a(a+1)(a+2)\cdots(a+k-1)$ with $(a)_0 = 1$.

Among others, the confluent hypergeometric function of the first kind satisfies the recurrence relations

$$\begin{aligned} (b-a) {}_1F_1(a-1; b; x) + (2a-b+x) {}_1F_1(a; b; x) - a {}_1F_1(a+1; b; x) &= 0 \\ b(b-1) {}_1F_1(a; b-1; x) + b(1-b-x) {}_1F_1(a; b; x) + x(b-a) {}_1F_1(a; b+1; x) &= 0 \\ (1+a-b) {}_1F_1(a; b; x) - a {}_1F_1(a+1; b; x) + (b-1) {}_1F_1(a; b-1; x) &= 0. \end{aligned} \quad (30)$$

Many of the commonly used functions are special instances of the confluent hypergeometric

function of the first kind. For example,

$${}_1F_1(a; a; x) = e^x \quad (31)$$

$${}_1F_1\left(\frac{1}{2}; \frac{3}{2}; -x^2\right) = \frac{\pi^{1/2}}{2x} \operatorname{erf}(x). \quad (32)$$

Finally, the asymptotic behavior of the function ${}_1F_1(a; b; x)$ as $|x| \rightarrow \infty$ when x is real, is given by

$$\begin{aligned} \frac{{}_1F_1(a; b; x)}{\Gamma(b)} &= \frac{e^{i\pi a} x^{-a}}{\Gamma(b-a)} \left[\sum_{n=0}^{R-1} \frac{(a)_n (1+a-b)_n}{n!} (-x)^{-n} + O(|x|^{-R}) \right] \\ &+ \frac{e^x x^{a-b}}{\Gamma(a)} \left[\sum_{n=0}^{S-1} \frac{(b-a)_n (1-a)_n}{n!} x^{-n} + O(|z|^{-S}) \right]. \end{aligned} \quad (33)$$

Appendix B. A_l and B_l Coefficients

Although the recursion relations of the confluent hypergeometric functions provided in Eqs. 30 are useful in seeing that the $I_l(\mathbf{u})$ functions can be expressed as the sum of two terms (one involving exponential and the other involving error functions as in Eq. 8), the derivation of the analytical form of the A_l and B_l coefficients using these recursion relations is a formidable task. Therefore, in order to find analytical expressions for the A_l and B_l coefficients for a general l value, we make a term-by-term comparison of the asymptotic form of the I_l function evaluated from Eq. 33 with the asymptotic form of Eq. 8. After some tedious algebra we have found that, if A_{ln} and B_{ln} are defined such that

$$A_l(\mathbf{u}) = \sum_{n=0}^{l/2} A_{ln} \beta(\mathbf{u})^{-2n} \quad \text{and} \quad B_l(\mathbf{u}) = \sum_{n=0}^{l/2-1} B_{ln} \beta(\mathbf{u})^{-2n}, \quad (34)$$

the following expressions hold:

$$A_{ln} = \begin{cases} A^0 & , \text{ if } n < 2 \\ A^0 + \sum_{t=1}^{n-1} \frac{(-1)^{t-1} (2t-3)!! \left(\frac{l+3}{2}\right)_{n-t-1} \left(1-\frac{l}{2}\right)_{n-t-1} (l+1)!!}{\Gamma(l/2)(n-t-1)! 2^{l/2-2n+t}} & , \text{ if } n \geq 2 \end{cases} \quad (35)$$

where $(l+1)!! = (l+1)(l-1)\cdots 1$ and

$$A^0 = \frac{(-1)^{l/2+n}}{n!} 2^{2n} \left(\frac{l}{2}\right)_n \left(-\frac{l}{2} - \frac{1}{2}\right)_n \quad (36)$$

and

$$B_{ln} = \frac{\left(\frac{l+3}{2}\right)_n \left(1-\frac{l}{2}\right)_n (l+1)!!}{\Gamma\left(\frac{l}{2}\right) n! 2^{l/2-1-2n}}. \quad (37)$$

We have verified using Mathematica that these expressions indeed yield the correct coefficients for the $I_l(\mathbf{u})$ functions.

Appendix C. Convergence of the Laplace Series for the Probability Profile

Theorem: The series given by (see Eq. 5)

$$P(R_0\mathbf{r}) = \sum_{l=0}^{\infty} \sum_{m=-l}^l (-i)^l Y_{lm}(\mathbf{r}) \int d\mathbf{u} Y_{lm}(\mathbf{u})^* I_l(\mathbf{u}) \quad (38)$$

is convergent.

Proof: We start by inserting the upper bound for the spherical Bessel functions of order l (Abramowitz and Stegun, 1977)

$$|j_l(2\pi q R_0)| \leq \frac{\sqrt{\pi}(\pi q R_0)^l}{2\Gamma(l + \frac{3}{2})} = \frac{(2\pi q R_0)^l}{(2l + 1)!!} \quad (39)$$

into Eq. 6. This yields the upper bound for the functions $I_l(\mathbf{u})$

$$I_l(\mathbf{u}) \leq \frac{(l + 1)!!}{(2l + 1)!! 2^{l/2} (4\pi D(\mathbf{u})t)^{3/2}} \left(\frac{R_0^2}{D(\mathbf{u})t} \right)^{l/2}. \quad (40)$$

Note that using the addition theorem for spherical harmonics (Arfken and Weber, 2001),

$$\sum_{m=-l}^l Y_{lm}(\mathbf{r}) Y_{lm}(\mathbf{u})^* = \frac{2l + 1}{4\pi} P_l(\mathbf{u} \cdot \mathbf{r}), \quad (41)$$

where $P_l(x)$ is the l -th order Legendre polynomial, it is possible to express Eq. 5 in the following form:

$$P(R_0\mathbf{r}) = \sum_{l=0}^{\infty} \varrho_l, \quad (42)$$

where

$$\varrho_l = \frac{(-i)^l (2l + 1)}{4\pi} \int d\mathbf{u} I_l(\mathbf{u}) P_l(\mathbf{r} \cdot \mathbf{u}). \quad (43)$$

Using the generating function for the Legendre polynomials, it is possible to prove that (Arfken and Weber, 2001)

$$|P_l(\cos \gamma)| \leq 1. \quad (44)$$

Using Eqs. 40 and 44, it is easy to see that

$$|\varrho_l| \leq \frac{(l + 1)!!}{(2l - 1)!! 2^{l/2} (4\pi D_{\min} t)^{3/2}} \left(\frac{R_0^2}{D_{\min} t} \right)^{l/2} = \xi_l, \quad (45)$$

where $D_{\min} = \min D(\mathbf{u})$. Note that

$$\lim_{l \rightarrow \infty} \frac{\xi_{l+2}}{\xi_l} = \lim_{l \rightarrow \infty} \frac{l + 3}{(2l + 1)(2l + 3)} \frac{R_0^2}{2D_{\min} t} = 0. \quad (46)$$

Therefore, using the d'Alembert (Cauchy) ratio test, the series $\sum_{l=0}^{\infty} \xi_l$ converges. Using the comparison test, it is straightforward to see that the series $\sum_{l=0}^{\infty} |\varrho_l|$ converges since $0 \leq |\varrho_l| \leq \xi_l$. Therefore, the series in Eq. 38 is absolutely convergent.

References

- Abramowitz, M., Stegun, I. A., 1977. Handbook of Mathematical Functions: With Formulas, Graphs, and Mathematical Tables. Dover Publications, New York.
- Alexander, D. C., Barker, G. J., Arridge, S. R., 2002. Detection and modeling of non-Gaussian apparent diffusion coefficient profiles in human brain data. *Magn Reson Med* 48 (2), 331–340.
- Arfken, G. B., Weber, H. J., 2001. Mathematical Methods for Physicists. Academic Press, San Diego.
- Assaf, Y., Freidlin, R. Z., Rohde, G. K., Basser, P. J., 2004. New modeling and experimental framework to characterize hindered and restricted water diffusion in brain white matter. *Magn Reson Med* 52 (5), 965–978.
- Basser, P. J., 2002. Relationships between diffusion tensor and q-space MRI. *Magn Reson Med* 47, 392–397.
- Basser, P. J., Mattiello, J., LeBihan, D., 1994a. Estimation of the effective self-diffusion tensor from the NMR spin echo. *J Magn Reson B* 103 (3), 247–254.
- Basser, P. J., Mattiello, J., LeBihan, D., 1994b. MR diffusion tensor spectroscopy and imaging. *Biophys J* 66 (1), 259–267.
- Basser, P. J., Pajevic, S., Pierpaoli, C., Duda, J., Aldroubi, A., 2000. In vivo fiber tractography using DT-MRI data. *Magn Reson Med* 44, 625–632.
- Callaghan, P. T., 1991. Principles of Nuclear Magnetic Resonance Microscopy. Clarendon Press, Oxford.
- Chenevert, T. L., Brunberg, J. A., Pipe, J. G., 1990. Anisotropic diffusion in human white matter: demonstration with MR techniques in vivo. *Radiology* 177 (2), 328–329.
- Cleveland, G. G., Chang, D. C., Hazlewood, C. F., Rorschach, H. E., 1976. Nuclear magnetic resonance measurement of skeletal muscle: anisotropy of the diffusion coefficient of the intracellular water. *Biophys J* 16 (9), 1043–1053.
- Conturo, T. E., Lori, N. F., Cull, T. S., Akbudak, E., Snyder, A. Z., Shimony, J. S., McKinstry, R. C., Burton, H., Raichle, M. E., 1999. Tracking neuronal fiber pathways in the living human brain. *Proc Natl Acad Sci* 96, 10422–10427.
- Frank, L. R., 2002. Characterization of anisotropy in high angular resolution diffusion-weighted MRI. *Magn Reson Med* 47 (6), 1083–1099.

- Inglis, B. A., Bossart, E. L., Buckley, D. L., Wirth, E. D., Mareci, T. H., 2001. Visualization of neural tissue water compartments using biexponential diffusion tensor MRI. *Magn Reson Med* 45 (4), 580–587.
- Jansons, K. M., Alexander, D. C., 2003. Persistent angular structure: new insights from diffusion magnetic resonance imaging data. *Inverse Problems* 19, 1031–1046.
- Liu, C. L., Bammer, R., Moseley, M. E., 2003. Generalized diffusion tensor imaging (GDTI): A method for characterizing and imaging diffusion anisotropy caused by non-Gaussian diffusion. *Isr J Chem* 43 (1–2), 145–154.
- Maier, S. E., Vajapeyam, S., Mamata, H., Westin, C. F., Jolesz, F. A., Mulkern, R. V., 2004. Biexponential diffusion tensor analysis of human brain diffusion data. *Magn Reson Med* 51 (2), 321–330.
- Mori, S., Crain, B. J., Chacko, V. P., van Zijl, P. C. M., 1999. Three-dimensional tracking of axonal projections in the brain by magnetic resonance imaging. *Ann Neurol* 45, 265–269.
- Moseley, M. E., Cohen, Y., Kucharczyk, J., Mintorovitch, J., Asgari, H. S., Wendland, M. F., Tsuruda, J., Norman, D., 1990. Diffusion-weighted MR imaging of anisotropic water diffusion in cat central nervous system. *Radiology* 176 (2), 439–445.
- Niendorf, T., Dijkhuizen, R. M., Norris, D. G., van Lookeren Campagne, M., Nicolay, K., 1996. Biexponential diffusion attenuation in various states of brain tissue: implications for diffusion-weighted imaging. *Magn Reson Med* 36 (6), 847–857.
- Özarslan, E., Mareci, T. H., 2003. Generalized diffusion tensor imaging and analytical relationships between diffusion tensor imaging and high angular resolution diffusion imaging. *Magn Reson Med* 50, 955–965.
- Özarslan, E., Vemuri, B. C., Mareci, T. H., 2004a. Generalized diffusion tensor imaging of excised rat brain. In: *Proc. of the 12th Scientific Meeting of ISMRM*. p. 92.
- Özarslan, E., Vemuri, B. C., Mareci, T. H., 2004b. Multiple fiber orientations resolved by generalized diffusion tensor imaging. In: *Proc. of the 12th Scientific Meeting of ISMRM*. p. 89.
- Özarslan, E., Vemuri, B. C., Mareci, T. H., 2005. Generalized scalar measures for diffusion MRI using trace, variance and entropy. *Magn Reson Med* 53 (4), 866–876.
- Pajevic, S., Pierpaoli, C., 1999. Color schemes to represent the orientation of anisotropic tissues from diffusion tensor data: application to white matter fiber tract mapping in the human brain. *Magn Reson Med* 42 (3), 526–540.

- Parker, G. J. M., Alexander, D. C., 2003. Probabilistic Monte Carlo based mapping of cerebral connections utilising whole-brain crossing fibre information. In: Taylor, C. J., Noble, A. (Eds.), *Information Processing in Medical Imaging (IPMI'03)*. Vol. 2737 of *Lecture Notes in Computer Science*. Springer, pp. 242–254.
- Ritchie, D. W., Kemp, G. J. L., 1999. Fast computation, rotation, and comparison of low resolution spherical harmonic molecular surfaces. *J Comput Chem* 20 (4), 383–395.
- Schwabl, F., 1989. *Quantum Mechanics*. Springer-Verlag, Berlin.
- Söderman, O., Jönsson, B., 1995. Restricted diffusion in cylindrical geometry. *J Magn Reson A* (117), 94–97.
- Stejskal, E. O., 1965. Use of spin echoes in a pulsed magnetic-field gradient to study anisotropic, restricted diffusion and flow. *J Chem Phys* 43 (10), 3597–3603.
- Stejskal, E. O., Tanner, J. E., 1965. Spin diffusion measurements: Spin echoes in the presence of a time-dependent field gradient. *J Chem Phys* 42 (1), 288–292.
- Tournier, J. D., Calamante, F., Gadian, D. G., Connelly, A., 2004. Direct estimation of the fiber orientation density function from diffusion-weighted MRI data using spherical deconvolution. *NeuroImage* 23, 1176–1185.
- Tuch, D. S., 2004. Q-ball imaging. *Magn Reson Med* 52, 1358–1372.
- Tuch, D. S., Reese, T. G., Wiegell, M. R., Makris, N., Belliveau, J. W., Wedeen, V. J., 2002. High angular resolution diffusion imaging reveals intravoxel white matter fiber heterogeneity. *Magn Reson Med* 48 (4), 577–582.
- Tuch, D. S., Reese, T. G., Wiegell, M. R., Wedeen, V. J., 2003. Diffusion MRI of complex neural architecture. *Neuron* 40, 885–895.
- Tuch, D. S., Weisskoff, R. M., Belliveau, J. W., Wedeen, V. J., 1999. High angular resolution diffusion imaging of the human brain. In: *Proc. of the 7th Annual Meeting of ISMRM, Philadelphia*. p. 321.
- von dem Hagen, E. A. H., Henkelman, R. M., 2002. Orientational diffusion reflects fiber structure within a voxel. *Magn Reson Med* 48 (3), 454–459.
- Wedeen, V. J., Reese, T. G., Tuch, D. S., Weigel, M. R., Dou, J. G., Weisskoff, R. M., Chessler, D., 2000. Mapping fiber orientation spectra in cerebral white matter with Fourier transform diffusion MRI. In: *Proc. of the 8th Annual Meeting of ISMRM, Denver*. p. 82.